Analogue modelling of basin inversion: the role of oblique kinematics and implications for the Araripe Basin (Brazil)

Pâmela C. Richetti[1,2], Frank Zwaan[2,3], Guido Schreurs[2], Renata S. Schmitt[1, 2, 4], Timothy C. Schmid[2]

5   [1] Programa de Pós-graduação em Geologia-PPGL, Universidade Federal do Rio de Janeiro, Brazil

[2] Institute of Geological Sciences, University of Bern, Bern, Switzerland

[3] Helmholtz Centre Potsdam - GFZ German Research Centre for Geosciences, Potsdam, Germany

[4] Departamento de Geologia-IGEO, Universidade Federal do Rio de Janeiro, Brazil

Correspondence: Pâmela C. Richetti (pamelarichetti@geologia.ufrj.br)

10   **Abstract.**

Basin inversion is a process that takes place when a sedimentary basin is subjected to compressional stresses and may result in the reactivation of pre-existing faults and/or the localization of deformation along new reverse faults. The Araripe Basin (NE Brazil) is an example of a Cretaceous intracontinental aborted rift with its sedimentary infill found at ca. 1000 m altitude in the present day. Post-rift basin inversion is

15   proposed as the cause of this topographic high, however how inversion mechanisms affected this basin is a matter of debate with two end member scenarios: reactivation of pre-existing normal faults leading to local uplift, or regional tectonic uplift. In this study, we conducted analogue models of basin inversion to test these scenarios. We present two series of crustal-scale brittle-viscous experiments: i) extension followed by compression without sedimentation, with a variation of rifting and inversion directions (orthogonal or

20   45˚ oblique) and ii) extension and compression with syn-rift sedimentation, with the same variation in rifting and inversion directions. We used a seed representing a structural weakness that was applied at the base of the brittle layer to localize deformation along the model axis. We found that orthogonal rifting without sedimentation forms through-going border faults, whereas oblique rifting creates initial en-echelon faults that eventually link up creating large border faults. Rift basins with syn-rift sedimentation evolved in

25   a similar fashion, however sedimentary loading increased subsidence. During inversion, most deformation is accommodated along new low angle reverse faults. Within that framework, significant intra-graben fault reactivation occurred in models without sedimentation. By contrast, syn-rift sedimentation caused only minor reactivation of rift faults in oblique inversion since the sediments acted as a buffer during compression; no rift fault reactivation occurred in orthogonal compression situations. Comparing the

30   existing scenarios for inversion in the Araripe Basin with our model results and field data show that these scenarios do not fully explain the natural example. Therefore, we propose an alternative scenario based on our models, involving oblique compression and the development of low angle reverse faults, which better explains inversion in the Araripe Basin.

1 Introduction

35   The tectonic inversion of sedimentary basins as a result of compressional tectonics is a widely discussed topic due to its importance for the development of mineral (Sibson and Scott, 1998) and hydrocarbon deposits (Turner and Williams, 2004). Especially inverted intraplate rift basins that are currently situated above sea level can play an important role for the understanding of their offshore equivalents, since they provide access to outcrops that otherwise can only be analyzed via indirect geophysical methods (e.g.,

40   Stanton et al., 2014; Rebelo et al., 2021).

In this context, the Araripe Basin in NE Brazil (Fig. 1), is an excellent example of an inverted intraplate rift basin. This Early Cretaceous rift basin is part of the aborted Brazilian Northeast Rift System (BNRS) (de Matos, 1992) located at the intersection of the equatorial and central segments of the South Atlantic Ocean (Moulin et al., 2010). This rift system formed within the well-developed network of NE-SW and E-W

45   striking Precambrian ductile shear zones in the basement of the Borborema Province (Fig. 1a) (Vauchez et al., 1995; Brito Neves et al., 2000; Ganade de Araujo et al., 2014). The rift structures of the Araripe Basin are mainly NE-SW and E-W (Fig.1a), indicating brittle reactivation of the basement shear zones (de Matos, 1992), especially the dextral reactivation of the E-W Patos Shear Zone bounding the north of the basin (Fig. 1a).

50   After rifting and subsequent thermal subsidence (Assine, 2007), the basin registered a phase of inversion (Fig. 1b) (Marques et al., 2014) and its sedimentary infill is presently situated, at its highest point, at 1000 m above sea level. Similarly, the Borborema Province contains high topographies and evidence of recent uplift (Lamarque and Julià, 2019; Neto et al., 2019). Other basins in the BNRS also present evidence of tectonic inversion (Vasconcelos et al., 2021; Bezerra et al., 2020). In the Araripe Basin, Marques et al.

55   (2014) proposed that inversion resulted from far-field ENE-WSW directed horizontal stress. They concluded that this deformation is consistent with the formation of new oceanic crust in the South Atlantic to the east and the development of the Andes to the west, resulting in overall compression of the South America plate.

According to Marques et al. (2014), this compression caused the complete inversion of the initial high angle

60   normal faults of the Araripe Basin (Fig. 1e) through an oblique compression and injection of soft material in these faults. By contrast, Peulvast and Bétard, (2015) proposed that the present-day topographic elevation of the basin is due to the regional uplift of the Borborema Province and the action of differential erosion (Fig. 1d). As such, the exact mechanism causing inversion, and to what degree rift structures were reactivated in the Araripe Basin remains unclear, requiring further research with new approaches. One of

65   these new approaches is the use of analogue modelling, which has shown to be a useful tool to understand the evolution of inverted basins and the mechanisms involved in various settings (Panien et al., 2005a; del Ventisette et al., 2005, 2006; Pinto et al., 2010a; di Domenica et al., 2014; Jara et al., 2018; Zwaan et al., 2022).

In this paper we present the results of new analogue modeling experiments aimed at evaluating whether

70   horizontal compression could indeed have caused the normal fault reactivation and full basin extrusion in the Araripe Basin as proposed by Marques et al. (2014), or whether regional uplift as proposed by Peulvast and Bétard (2015) forms a better explanation. In our models we test the influence of orthogonal (α=0) or

oblique (α=45°) extension, followed by either orthogonal or oblique compression, as well as syn-rift sedimentation on rift development and on subsequent inversion structures. We then compare our model results with the Araripe inversion models by Marques et al. (2014) and Peulvast and Bétard (2015) and propose a new interpretation of how inversion took place in the basin.
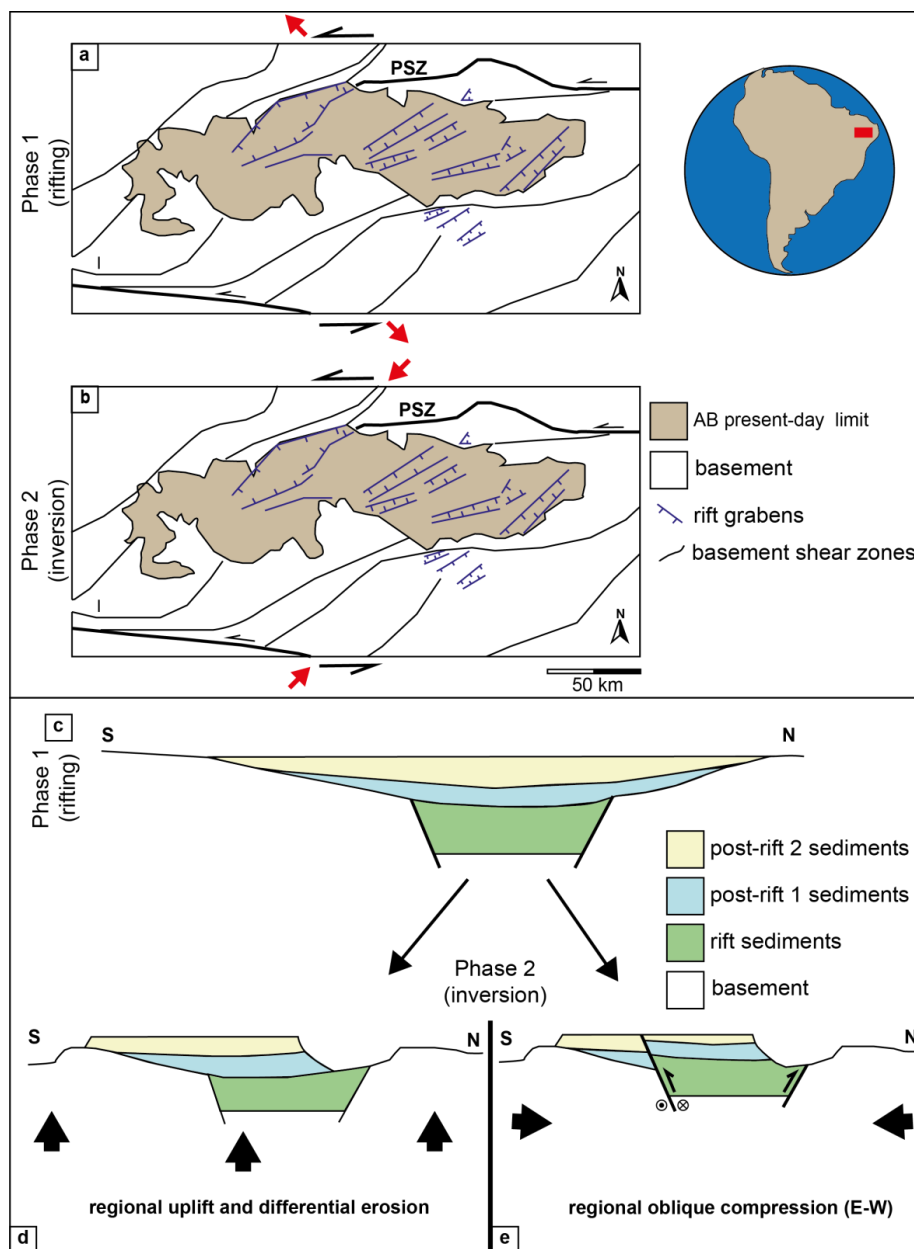
Figure 1: Structural geology of the study area and present-day Araripe Basin. (a) NE-SW rift related structures (in blue) and Precambrian basement shear zones (in black), modified after Camacho and de Oliveira E Sousa (2017). PSZ: Patos Shear Zone. b) Inversion kinematics after Marques et al. (2014). c) Schematic N-S cross-section representing rift and post rift formations in the Araripe Basin prior to inversion. d) Schematic representation of the Araripe Basin inversion model based on regional uplift followed by differential erosion proposed by Peulvast and Bétard (2015). e) Schematic representation of the Araripe Basin inversion model as a result of regional oblique compression proposed by Marques et al. (2014).

2 Methods

2.1 Model set up

For this study of crustal-scale basin inversion processes, we used an experimental set-up involving two long mobile sidewalls, two rubber sidewalls (fixed between the mobile walls, closing the short model ends), and a base consisting of a mobile and a fixed base plate (Fig 2a). We positioned a 5 cm high block consisting of an intercalation of foam (1 cm thick) and Plexiglas (0.5 cm thick) bars above the base plates and between the long sidewalls (Fig. 2a,b). This foam/Plexiglas block, initially 36.5 cm wide, was compressed prior to adding the model materials in order to reach the initial experiment width of 30 cm (Fig. 2a,b). This set-up has been regularly used for orthogonal and oblique rifting and compression models (Schreurs and Colletta, 1998, 2002; Zwaan and Schreurs, 2017; Zwaan et al., 2016, 2018a, 2020; Schmid et al, 2022a, b). The divergence of the mobile sidewalls, achieved by high-precision computer-controlled motors, simulates an initial rifting phase inducing uniform orthogonal extension into the overlying brittle and viscous model materials that represent the brittle upper crust and ductile lower crust, respectively. For orthogonal convergence during the subsequent inversion phase, the sidewalls are simply moved together again. During oblique divergence and oblique convergence, additional lateral motion of the mobile base plate on one side of the experiment was applied (Fig. 2c).

In order to localize deformation in our models, creating a graben during the initial rifting phase, we introduce a linear seed on the top of the viscous layer that was made from the same viscous material as used for the lower crustal layer (e.g. Le Calvez & Vendeville 2002; Molnar et al., 2019, 2020; Zwaan and Schreurs, 2017). This seed was a semi-cylindrical ridge with a c. 1 cm diameter, and was placed in the same position in each model (i.e. along the central axis of the model, Fig 2a,b).
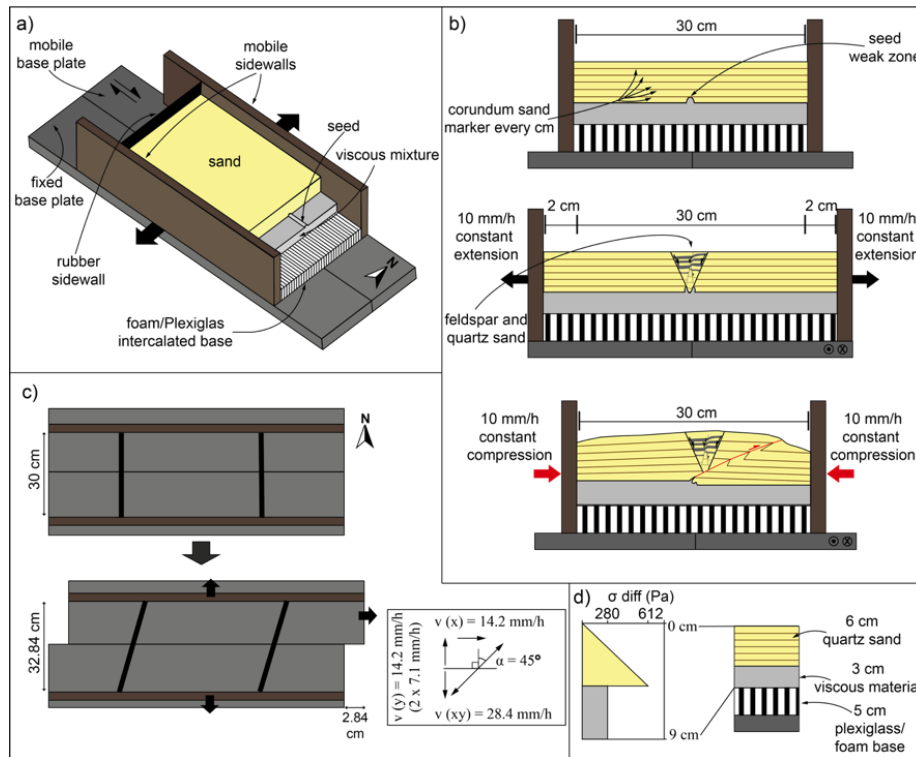
Figure 2: Experimental set-up adopted for this study. a) 3D cut-out view showing the brittle-viscous layers on top of the Plexiglas/foam base of the experiment (north arrow added for reference in the models). b) Schematic example of a sedimentation model run in 2D. c) Top view example of movement direction of the experimental apparatus used in this study (oblique extension example, with definition of divergence and compression obliquity as angle α). d) Schematic strength profile indicating the crustal setting represented in our models.

2.2 Materials

We utilized brittle and viscous analogue materials (material properties summarized in Table 1) to reproduce the brittle and ductile parts of the upper and lower crust in our experiments.

A 3 cm thick viscous layer served to replicate a 10 km thick lower crust. This material consists of a near-Newtonian (η = ca. $1.5 \cdot 10^5$ Pa · s ; n = 1.05-1.10, Zwaan et al., 2018c) mixture of SGM-36 Polydimethylsiloxane (PDMS) and corundum sand ($\rho_{specific}$ = 3950 kg/m^3, https://www.carloag.ch). We mixed the components according to a 0.965: 1.00 weight ratio, resulting in a viscous mixture with a density of ca. 1600 kg/m^3.

We applied a 6 cm thick layer of fine quartz sand (ø = 60-250 µm, and ϕ = 31.4-36.1˚, Table 1) sieved on top of the viscous layer, representing a 20 km brittle upper crust (Zwaan et al. 2018a). The sand was flattened at 1 cm intervals with a scraper to avoid lateral variation in sand layer thickness during the model preparation. We sieved the sand from ca. 30 cm height to ensure a constant brittle layer density of ca. 1560 kg/m^3 (e.g. Klinkmüller et al., 2016; Schmid et al., 2020).

We used layers of feldspar sand (ø = 100-250 mu) intercalated with layers of quartz sand for sedimentary infill in order to provide a visual record of syn-rift units on cross-sections (Fig. 2b). The sand application was done by hand, using a paper cone with an opening of 3 mm at the tip. The flux of sand was controlled by pressing the opening of the cone and we filled the graben up to the general model surface. The use of feldspar sand as syn-rift sediment is not considered to significantly impact model evolution due to the very similar characteristics to our quart sand (Zwaan et al., 2022).

Furthermore, we added thin <1 mm thick marker intervals of fine corundum sand (ø = 88-125 mu) to the quartz sand layer, which allowed for the tracing of deformation in cross-section (Fig. 2b). These thin intervals were sieved in during the scraping intervals (every cm) and are not considered to have an impact on model evolution.

Table 1: Materials properties

Granular materials	Quartz sand[a]	Corundum sand[b]	Feldspar sand[h]
Grain size range (ø)	60-250 μm	88-125 μm	100-250 μm
Specific density ($\rho_{specific}$)[c]	2650 kg/m^3	3950 kg/m^3	ca. 2700 kg/m^3
Sieved density (ρ_{sieved})	1560 kg/m^3	1890 kg/m^3	ca. 1300 kg/m^3
Angle of internal peak friction (ϕ_{peak})	36.1°	37°	35°
Coefficient of internal peak friction (μ_{peak})[d]	0.73	0.75	0.70
Angle of dynamic-stable friction (ϕ_{dyn})	31.4°	32.0°	29.9°
Coefficient of dynamic-stable friction (μ_{dyn})[d]	0.66	0.62	0.58
Angle of reactivation friction (ϕ_{react})	33.5°	-	32.0°
Coefficient of reactivation friction (μ_{react})	0.66	-	0.62
Cohesion (C)	9 ± 98 Pa	39 ± 10 Pa	51 Pa

Viscous material	Pure PDMS[a,e]	PDMS/corundum sand mixture[a]	
Weight ratio PDMS : corundum sand	-	0.965 kg : 1.00 kg	
Density (ρ)	965 kg/m^3	ca. 1600 kg/m^3	
Viscosity (η)	ca. 2.8 · 10^4 Pa.s	ca. 1.5 · 10^5 Pa.s [f]	
Type[f]	Newtonian (n = ca. 1)[g]	near-Newtonian (n = 1.05-1.10)[g]	

a Quartz sand, PDMS and viscous mixture characteristics after Zwaan et al. (2016; 2018a, 2018b)
b Corundum sand characteristics after Panien et al. (2006)
c Specific densities after Carlo AG (2022)
d   μ = tan (φ)
e Pure PDMS rheology details after Rudolf et al. (2016)
f Viscosity value holds for model strain rates < 10-4 . s^{-1}
g Power-law exponent n (dimensionless) represents sensitivity to strain rate
h Feldspar sand characteristics after Zwaan et al. (2022)

140

2.3 Model parameters

For this study we completed two main series of four experiments each, and an initial series of reference experiments (Table 2). Series A contains our reference experiments that simulated the initial (orthogonal) rifting phase only, with and without syn-rift sedimentation. Series B explores the effects of basin inversion without syn-rift sedimentation. Series C tests the effects of syn-rift sedimentation during graben inversion. The initial rifting phase of our Series B and C basin inversion models involved either orthogonal or 45° oblique divergence (where obliquity is defined by angle alpha, i.e. the angle between the normal to the rift axis and the divergence direction, Fig. 2c). The subsequent phase of shortening involved either orthogonal or 45° oblique convergence (Table 2). The experiments ran for 2 hours with 40 mm of divergence (at 20 mm/h) and another 2 hours with 40 mm of convergence, except for Models B3 and C3 since the initial oblique opening did not generate sufficient space for a subsequent 40 mm of orthogonal divergence.

We implemented syn-rift sedimentation in 5 experiments (in Model A2 and in Models C1-4), by halting the machine every 15 min (8 intervals total) and filling the accommodation space by hand (pouring) with feldspar and quartz sand in alternating intervals (Fig. 2b). The two experiments with oblique rifting have only 7 sedimentation intervals because after the first 15 minutes, insufficient accommodation space was available, requiring us to start the first sand filling after 30 minutes instead.

Table 2: Parameters of analogue models performed in this study

Model Series	Model Name	Direction and velocity of divergence/convergence				Sedimentation	Cross-sections made
		Phase 1 (40 mm of divergence)		Phase 2 (40 mm of convergence)			
		Direction (angle α)	Velocity (v) mm/h	Direction (angle α)	Velocity (v) mm/h		
Series A Reference rifting models	A1	0°	20	-	-	No	Yes
	A2	0°	20	-	-	Yes	Yes
Series B Rifting and inversion	B1	0°	20	0°	20	No	Yes**
	B2	0°	20	45°	20	No	No
	B3*	45°	20	0°	20	No	No
	B4	45°	20	45°	20	No	No
Series C Rifting and inversion with sedimentation	C1	0°	20	0°	20	Yes	Yes
	C2	0°	20	45°	20	Yes	Yes
	C3*	45°	20	0°	20	Yes	Yes
	C4	45°	20	45°	20	Yes	Yes

* Models with reduced inversion time due to the oblique extension with reduced orthogonal opening.

** Sections not used in this paper

160   **2.4 Scaling**

Model scaling is important to guarantee that experiments completed in the laboratory are representative of natural examples. For the brittle materials, the main parameter is the angle of internal friction (35°-37°), which is similar to internal friction angle values found in the upper crust (31°-38°, Byerlee, 1978, Table 3). In order to scale the viscous material, we must consider its strain rate-dependent rheology. The stress ratio

165   between model and nature (σ^*, convention: $\sigma^* = \sigma_{model} / \sigma_{nature}$) is calculated as follows: $\sigma^* = \rho^* \cdot h^* \cdot g^*$, where ρ^*, h^* and g^* represent density, length, and gravity ratios, respectively (Hubbert, 1937; Ramberg, 1981). Combined with the viscosity ratio (η^*), the stress ratio yields the strain rate ratio $\acute{\epsilon}^*$ (Weijermars and Schmeling, 1986): $\acute{\epsilon}^* = \sigma^*/\eta^*$. Subsequently, the velocity and time ratios (v^* and t^*) are derived from the strain rate ratio: $\acute{\epsilon}^* = v^*/h^* = 1/t^*$. We adopt a relatively high lower crustal viscosity of ca. $5 \cdot 10^{21}$,

170   representing a typical early magma-poor rift system (e.g. Buck, 1991). Thus, one hour in our model represents ca. 1.3 Myr in nature, and 20 mm/h of extension/compression rate in the model embodies a realistic deformation velocity of ca. 5 mm/yr in nature. The scaling parameters are presented in Table 3.

The dynamic similarity of the model and natural example can also be examined. Firstly, the dynamic similarity between the model brittle layer and its upper crustal equivalent can be determined through the

175   ratio Rs between the gravitational stress and the cohesive strength or cohesion C (Ramberg, 1981; Mulugeta, 1988): R_s = gravitational stress/cohesive strength = $(\rho \cdot g \cdot h)/C$. A 9 Pa cohesion in the sand and a natural cohesion of 5 MPa for upper crustal rocks, gives us a Rs of 102 and 110 for model and nature, respectively. Secondly, the dynamic similarity between our viscous material and lower crust equivalent is derived from the Ramberg number Rm (Weijermars and Schmeling, 1986): R_m = gravitational

180   stress/viscous strength = $(\rho \cdot g \cdot h^2)/(\eta \cdot v)$, and both have the value of 68. We consider our models properly scaled since the Rs and Rm values are the same as their natural equivalent.

Table 3: Scaling parameters

		Model	**Nature**
General parameters	Gravitational acceleration (g)	9.81 m/s^2	9.81 m/s^2
	Divergence velocity (v)	$5.6 \cdot 10^{-6}$ m/s	$1.7 \cdot 10^{-10}$ m/s
Brittle layer	Material	Quartz sand	Upper crust
	Peak internal friction angle	$35°$-$37°$	31-$38°$
	Thickness (h)	$6 \cdot 10^{-2}$ m	$2 \cdot 10^{4}$ m
	Density	1560 kg/m^3	2800 kg/m^3
	Cohesion (C)	9 Pa	$5 \cdot 10^{6}$ Pa
Viscous/ductile layer	Material	PDMS/corundum sand mixture	Lower crust
	Thickness (h)	$3 \cdot 10^{-2}$ m	$1 \cdot 10^{4}$ m
	Density	1600 km/m^3	2900 kg/m3
	Viscosity	$1.5 \cdot 10^{5}$ Pa·s	$1 \cdot 10^{21}$ Pa·s
Dynamic scaling values	Brittle stress ratio (R$_s$)	102	110
	Ramberg number (R$_m$)	68	68

185

2.5 Model monitoring and analysis

The experiments were primarily monitored through time-lapse photographs of the model surface, taken every minute for the duration of the model run. One central camera (Nikon D810, 36 MPx) provided map view pictures, while two obliquely oriented cameras (D810 36 MPx) were positioned on both sides of the central one to provide stereoscopic imagery. The central camera was controlled using the Nikon Camera Control Pro software and cameras for stereoscopic imagery were remotely triggered by passing on the signal from the central camera via an ESPER Triggerbox (Schmid et al., 2022).

To facilitate the first order of surface deformation analysis, we sieved a thin grid (4 by 4 cm) of corundum sand on the model surface. We furthermore sprinkled the model surface with coffee powder to provide markers for later Digital Image Correlation (DIC) analysis. For the models involving syn-rift sedimentation, a fine layer (< 1 mm) of quartz sand was sieved on the top of the experiment at the end of rifting phase to create a blank surface for a new grid and new coffee markers, allowing for optimal tracing of deformation during the inversion phase. Note that we defined a North reference in the model apparatus in order to facilitate description of the results (Fig. 2)

To quantify and visualize the surface deformation evolution of the experiments, we applied a detailed analysis of the time-lapse photographs through DIC technique (e.g. Adam et al., 2005; Boutelier et al., 2019; Marshak et al., 2019; Zwaan et al., 2021; Schmid et al., 2022). The DIC analysis was performed by comparing top view images of subsequent time steps using LaVision's DaVis software (version 10.2). We used a calibration plate with a cross pattern of known dimensions as a reference to unwarp and rectify images and scale calculated displacements. Maximum and Minimum normal strains are defined as the magnitude of the largest (i.e., stretching) and smallest (i.e., shortening) axes of the strain ellipse, and are independent of coordinate orientation (e.g. Broerse et al., 2021). It is therefore a suitable marker to quantify extensional and compressional deformation in our experiments.

To reconstruct the model topography in detail, we used the pair of high-resolution oblique photographs for selected time steps. Agisoft Photoscan photogrammetry software served to merge this pair of synchronous photographs, using marked coordinates in the experiment for geo-referencing, and to create digital elevation models (DEMs) for the end of Phase 1 and 2. The DEMs, shown in map view, as well as the extracted topography profiles over time, are combined with the PIV results for a complete interpretation of model evolution (e.g. Maestrelli et al., 2020; Zwaan et al., 2022).

Finally, cross-sections were made to reveal the internal structures of the models at the end of the model run (at the end of the rifting phase for Series A models, and after inversion for Series B and C). In order to produce these cross-sections, we added water with soap at the edges of the model until the sand was saturated and stable, and cut 6 sections orthogonal to the model axis, each 10 cm apart. Pictures were taken for analysis of internal structures, and the quantification of subsidence. The cross-sections of the reference models (Series A) provide insights into the graben structure prior to inversion.

3 Results

225   The results of our model analysis are presented in summary figures for each experiment (Figs. 3-8). We show the incremental maximum and minimum normal strain from the DIC analysis for the early stage (first 30 minutes) and end stage of each phase (90-120 minutes interval), topography maps for the end of each deformation phase, and topographic profiles over 30 minutes increments. Model cross-sections are presented for Series A and C, and for one model in series B (Model B1).

230

3.1 Series A – Reference models

The Series A models provided a reference for the Series B and C analysis. These models had a constant divergence direction ($\alpha = 0°$) and -velocity of 20 mm/h (Fig. 3).

235   **3.1.1 Orthogonal rift without syn-rift sedimentation - Model A1**

Extensional deformation became highly localized in the first 30 minutes of the Model A1 run (Fig. 3a), forming two graben boundary faults rooting in the viscous seed (Fig.3i$_{I-III}$), which accommodated extension in one E-W striking graben. Towards the end of the rifting phase (Fig. 3b), a second-generation intra-graben fault developed between the two conjugate graben boundary faults. The strain analysis indicates higher

240   strain values in the southern graben border fault and within the second-generation intra-graben fault. However, the northern graben border fault remained active until the end of the experiment. Cross-section view show drag folds related to the northern and southern graben boundary faults (Fig. 3i). The final topography profiles (Fig. 3d; 60 min, 90 min and 120 min) show a vale topography on the southern side of the graben floor. This topographic feature can be related to the drag fold of the southern graben block in

245   cross-section view (Fig. 3i$_{II}$), indicating that the drag fold initiated after the first hour of experiment and continued evolving until the end of rifting phase. In the middle cross-section (Fig. 3i$_{II}$), we measured graben width between the two grabens border faults and the value is 56.2 mm. To measure the total fault offset, we used the uppermost corundum sand marker that showed a vertical downward displacement of 19.2 mm in total.

250

3.1.2 Orthogonal rifting with syn-rift sedimentation – Model A2

At early rifting stages of Model A2, strain analysis shows the concentration of deformation at the graben boundary faults (Fig. 3e). However, the maximum normal strain values are lower inside the graben (Fig. 3e,f) than observed in Model A1 (Fig. 3a,b). Later in the experiment, strain was homogeneously distributed

255   between the boundary faults and the set of conjugate faults in the middle of the graben (Fig. 3f,j). The syn-rift sedimentation (Fig. 3j) caused an increase of graben width and subsidence compared to the rifting phase without sedimentation (Fig. 3i): the offset of the first corundum sand marker shows a difference of ~1 cm between Model A1 (19.2 mm; Fig. 3i$_{II}$) and A2 (30.9 mm; Fig. 3j$_{II}$), and the graben structure was ~1 cm wider in Model A2 (65.2 mm) than in Model A1 (56.2 mm).
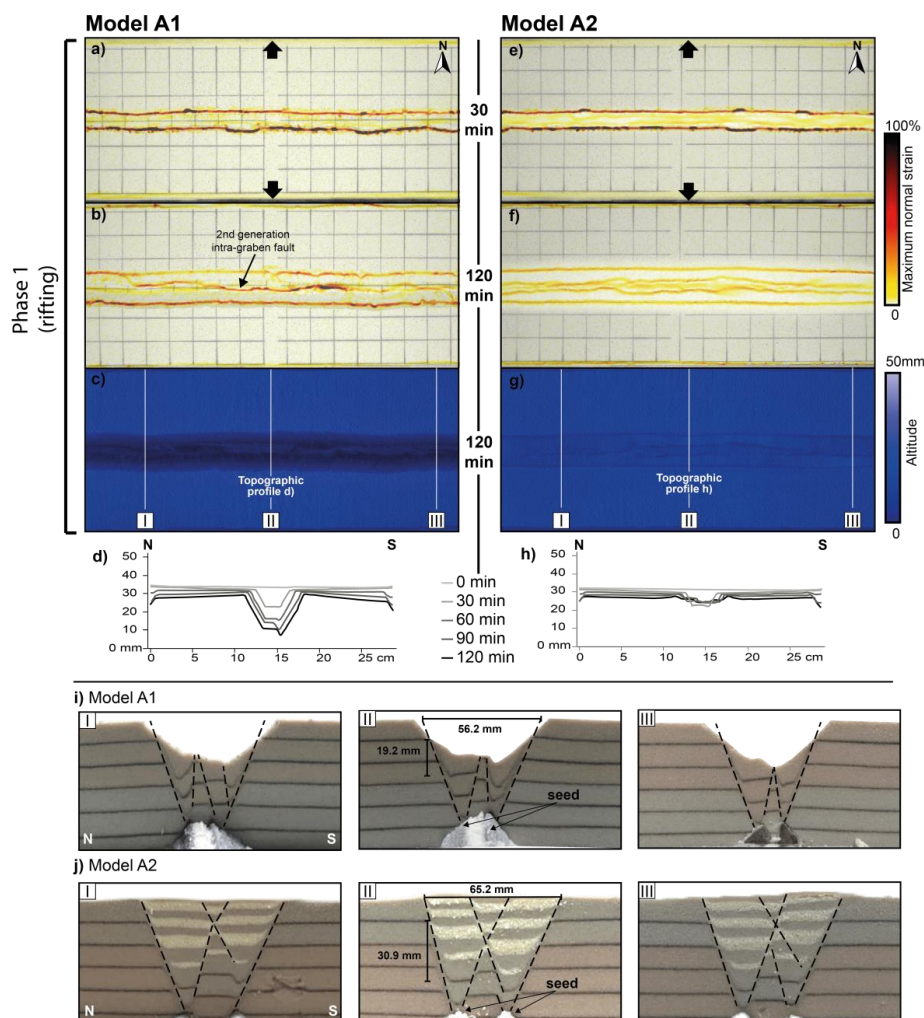
Figure 3: Evolution of deformation during rifting for Models A1 and A2. a) and b) displays top view model DIC analysis for Maximum normal strain at early and late rifting stage. c) Digital elevation model for late rifting stage. d) Topographic profiles for every 30 minutes of rifting. e) and f) display top view model DIC analysis for Maximum normal strain at early and late rifting stage. g) Digital elevation model for late rifting stage. h) Topographic profiles for every 30 minutes of rifting. Note that topography is shown prior to syn-rift sedimentation for that interval. i-j) Cross-sections from (i) Model A1 and (j) Model A2, respectively. Section locations are indicated in (b) and (f). Graben geometry measurements are indicated in the middle cross-sections.

3.2 Series B – inversion without sedimentation

Here we show the results for the series B models that underwent two deformation phases (rifting and inversion) but without syn-rift sedimentation. We first present Models B1 and B2 that involved orthogonal rifting, followed by Model B3 and B4 with oblique rifting. These model pairs between then underwent either orthogonal or oblique inversion.

3.2.1 Orthogonal rifting - orthogonal (B1) and oblique inversion (B2)

275

The results from Models B1 and B2 show very similar outcomes between them after phase 1 and are also very similar to reference Model A1 (Figs. 3a-b; 4a-b and i-j). Early rifting (Fig. 4a and i) localized more strain along the graben normal faults than in the later rift phase; during the late rift stage (Fig. 4b and j), strain was distributed between the graben boundary faults and the intra-graben faults. The topography

280 analysis (Fig. 4c, g, k and o) shows a graben subsidence of ~20 mm.

During the orthogonal inversion phase, Model B1 initially localized strain both along the intra-graben faults and along new reverse faults on both sides of the graben (Fig. 4d). Towards the end of the model run, most parts of the southern reverse fault became relatively inactive while the northern reverse fault grew and localized higher strain (Fig. 4e). At this stage, also the intra-graben faults had become inactive (Fig. 4e).

285 The areas immediately adjacent north and south to the graben were uplifted, while the bottom of the inverted graben reached the same elevation as the pre-rift surface (Fig. 4f, h).

After the first hour of oblique inversion in Model B2, strain was localized along the graben border faults (Fig. 4l) showing direct reactivation of the original graben faults only, in clear contrast to the orthogonal inversion of Model B1 (Fig. 4d). At the end of Phase 2, however, a single oblique reverse fault had appeared

290 at the model surface grid, north of the graben, while all previous rift related faults were inactive (Fig. 4m). The final topography shows a significantly higher maximum elevation than the pre-rift surface of ~15 mm in orthogonal inversion Model B1 (Fig. 4f, h), while the oblique inversion Model B2 (Fig. 4n, p) had an ~7 mm higher elevation than the pre-rift surface.
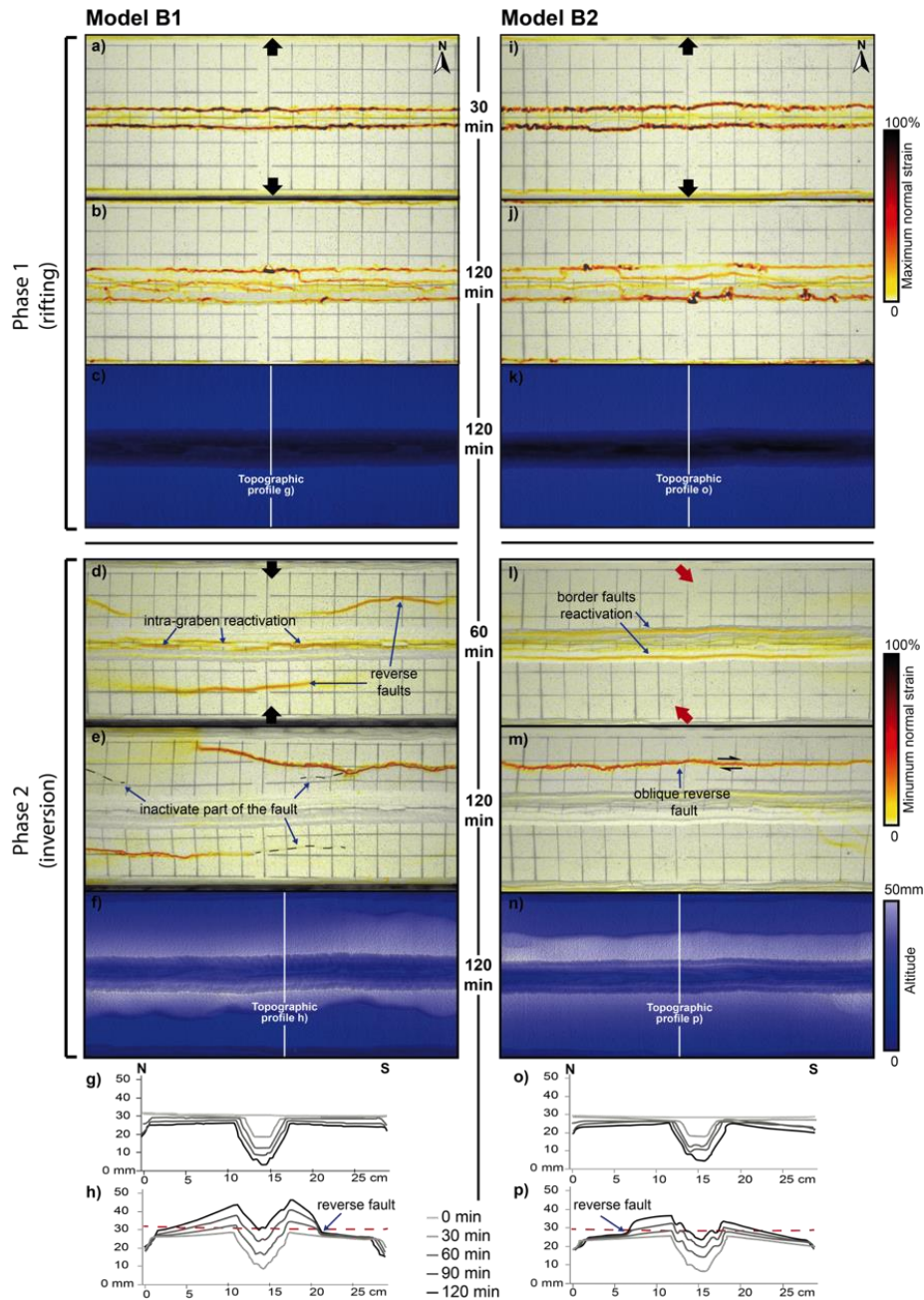
Figure 4: Evolution of deformation during rifting and inversion for Models B1 and B2. a) and b) displays top view model DIC analysis for Maximum normal strain at early and late rifting stage. c) Digital elevation model for late rifting stage. d) and e) displays top view model DIC analysis for Minimum normal strain. f) Digital elevation model for late inversion stage. g, o) Topographic profiles for every 30 minutes of rifting phase. h, p) Topographic profiles for every 30 minutes of inversion phase. The red horizontal line indicates the initial surface level at the start of the model run.

3.2.2 Oblique rifting - orthogonal (B3) and oblique inversion (B4)

Models B3 (Fig. 5a) and B4 (Fig. 5i), with 45° oblique rifting, resulted in the development of two bands of *en echelon* normal faults bounding a graben after the first 30 minutes of deformation. At the end of Phase 1, the strain results shows that these *en echelon* faults had become interconnected, forming through-going graben-bounding normal faults, connected by lower strain diagonal zones within the graben (Fig. 5b,j).

The orthogonal inversion of Model B3 resulted in the activation of a new straight fault along the central axis of the graben and the formation a new reverse fault south of the graben (Fig. 5d,e). By the end of the inversion phase, the reverse fault remained active while the fault in the middle of the graben started became less active, with some parts being completely inactive (Fig. 5e). Uplift was more prominent in the area between the reverse fault and the graben, while in the northern part of the experiment a more widespread uplift is recorded (Fig. 5f, g).

After the first hour of oblique inversion in Model B4, the diagonal graben structures were partially reactivated, while a significant portion of the deformation localized in a new reverse fault to the north of the graben, and deformation started to localize in the southern area of the experiment as well (Fig. 5l). During the later stages of inversion, the northern reverse fault became almost completely inactive, and deformation localized on the southern reverse fault (Fig. 5m). The map view grid analysis showed the oblique movement of the reverse faults (Fig. 5m). Rift faults concentrated minor reactivation and became almost completely inactive by the end of the inversion phase (Fig. 5m). The topography profiles indicate uplift of the rift structures (17 mm elevation of the bottom of the graben) and the new reverse faults on both sides of it (Fig 5p), and while the northern reverse fault became inactive, widespread uplift affected the northern part of the model (Fig. 5p). Along the topography profile, the maximum uplift not related to the reverse faults was 5 mm in the north (where the fault became inactive) and 2 mm in the south.
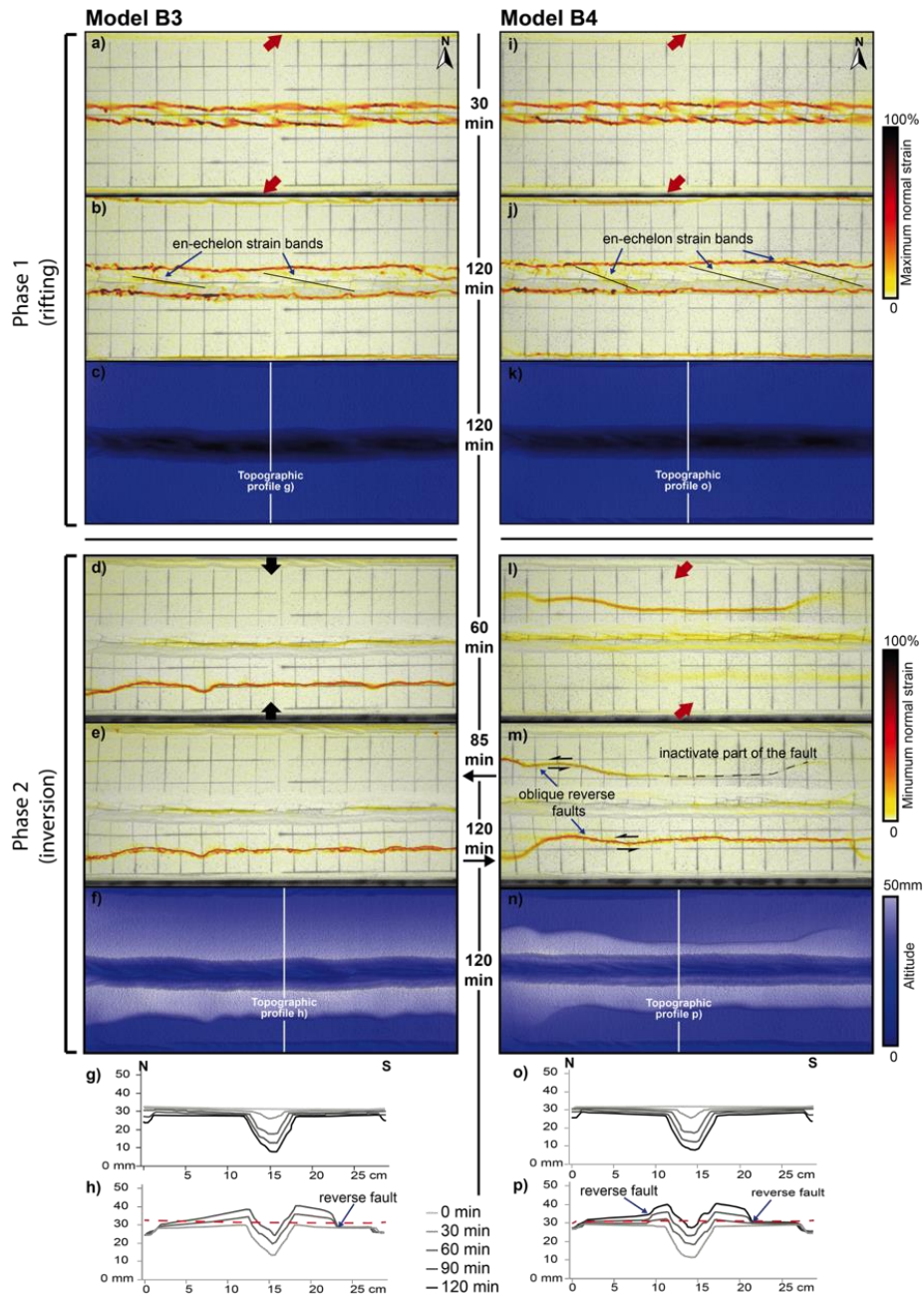
Figure 5: Evolution of deformation during rifting and inversion for Models B3 and B4. a, i), and b, j) display top view model DIC analysis for Maximum normal strain at early and late rifting stage, resp. c, k) Digital elevation model for late rifting stage. d, l,) and e, m) display top view model DIC analysis for Minimum normal strain. f and n) Digital elevation model for late inversion stage. g and o) Topographic profiles for every 30 minutes of rifting phase. h and p) Topographic profiles for every 30 minutes of inversion phase. Model B3 has a reduced inversion time of 85 minutes instead of 120 minutes, as indicated in the figure.

3.3 Series C – inversion with sedimentation

Here we present the results for our Series C models with rifting phase divided in 8 sedimentation intervals of 15 minutes each, with 20 mm/h of displacement during rifting and subsequence convergence. The results are presented in pairs according to the models' initial divergence direction (orthogonal and oblique, or $\alpha = 0°$ and $\alpha = 45°$) (Figs. 6, 8).

3.3.1 Orthogonal rifting with sedimentation - orthogonal (C1) and oblique inversion (C2)

The early stages of rifting of both Models C1 and C2 resulted in high strain localization in the graben border faults and lower strain rates inside the graben (Fig. 6a,i). During later rifting stages, the maximum normal strain values were lower along the graben border faults and instead rather evenly distributed among all faults within the graben (Fig. 6b,j). The results for the early and late stages of rifting show great similarity to the ones in Model A2 (Fig. 3e,f). Cross-section thickness measurements from each of the 15 minutes syn-rift sedimentation intervals (I1-I8), indicate a progressive increase of subsidence in the first two sedimentation intervals (Fig. 7a$_I$; I1 to I3). From interval I4 to I8, we observed a decrease in the subsidence rate.

The orthogonal inversion (Model C1, Fig. 6d-e) concentrated deformation on a new reverse fault at the southern part of the model. Strain data show high localization along this reverse fault, while no reactivation at all is visible in the previous rifting structures. In cross-section view (Fig. 7a$_{I,II}$) it becomes clear that the graben was uplifted by the reverse fault while the model surface was folded. This resulted in a curved and thick shear zone along the reverse fault that was seeded in the viscous layer, the latter which rose during rifting (Fig. 7a).

Compared to Model C1, oblique inversion shows a different effect on the reactivation of previous rift structures in Model C2 (Fig. 6l-m). We observe minor reactivation of the previously formed normal faults during the subsequent 45° oblique inversion phase, and main strain localization along reverse faults in the NW and SE, connected by strain localization zones parallel to the inversion direction. The topography analysis show a small (~2 mm) pop-up structure related to the graben border faults with small strike-slip component in the surface grid (Fig. 6n,p). In cross-section view, the reverse faults were in fact thicker shear zones in those locations where only one of them developed, whereas the shear zones were thinner when multiple reverse faults developed (Fig. 7b).
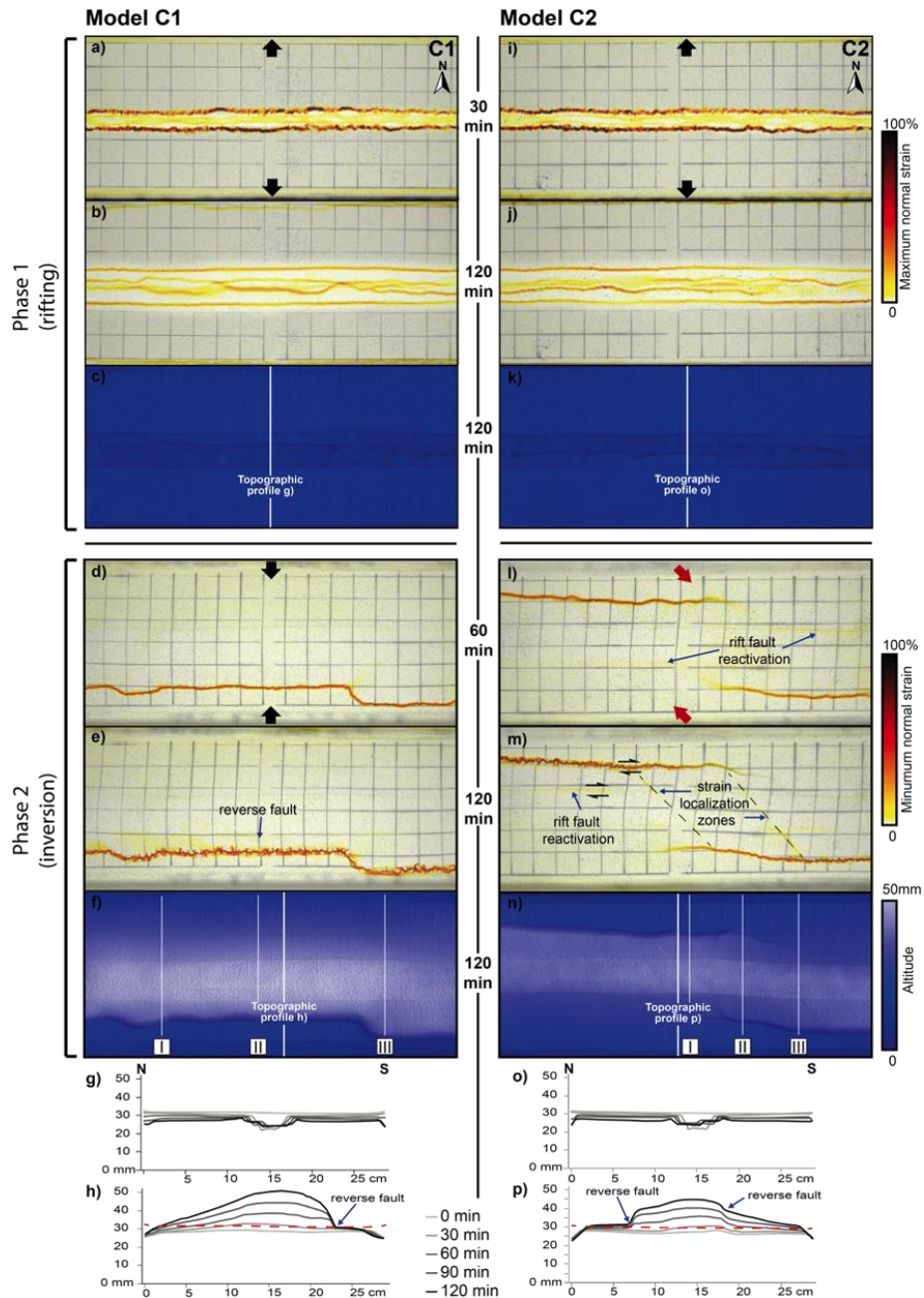
Figure 6: Evolution of deformation during rifting and inversion for Models C1 and C2. a) and b) displays top view model DIC analysis for Maximum normal strain at early and late rifting stage. c) Digital elevation model for late rifting stage. d) and e) displays top view model DIC analysis for Minimum normal strain. f) Digital elevation model for late inversion stage. g) Topographic profiles for every 30 minutes of rifting phase. h) Topographic profiles for every 30 minutes of inversion phase.

365
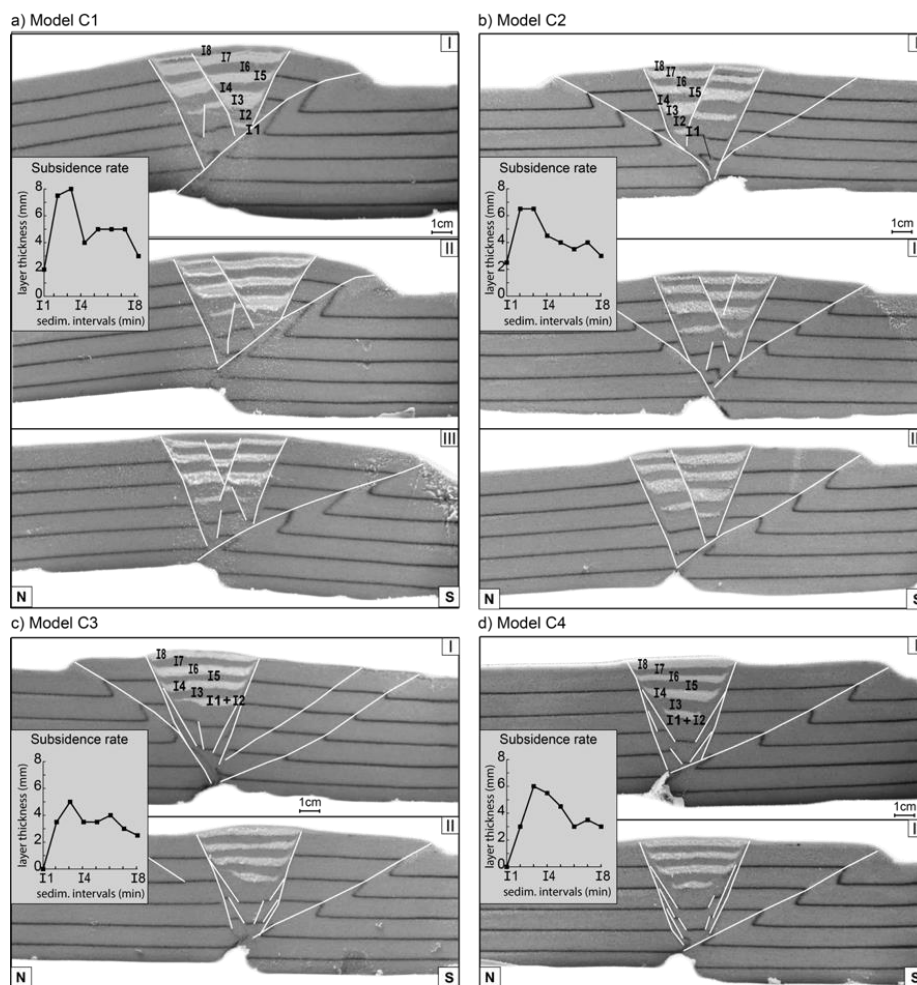
Figure 7: Cross-sections of experiments with sedimentation and measurements on models showing the influence of extension obliquity on sedimentation and subsidence rate. a) Model C1 with orthogonal extension and orthogonal inversion phases. b) Model C2 with orthogonal extension and oblique inversion phases. c) Model C3 with oblique extension and orthogonal inversion phases. d) Model C4 with oblique extension and orthogonal inversion phases. Section locations are shown in Figs. 5 and 7. Syn-rift units always starts with feldspar sand (white) and are divided into 8 intervals of 15 minutes of extension, except the oblique extension models (C3 and C4) that I1 and I2 are represented in the same unit. I1 = 15 min, I2 = 30 min, I3 = 45 min, I4 = 60 min, I5 = 75, I6 = 90 min, I7 = 105 min, I8 = 120 min. North (N) and South (S) references indicated at the bottom section of each model.

3.3.2 Oblique rifting with sedimentation – orthogonal (C3) and oblique (C4) inversion

Models C3 (Fig. 8a) and C4 (Fig. 8i) presented *en echelon* boundary faults after the first 30 minutes of experiment in response to the 45° oblique rifting, thus showing a similar result as Models B3 and B4 (Fig. 5b, i). After two hours of rifting the *en echelon* faults evolved into two main graben boundary faults, but some faint en echelon strain bands remained active within the graben (Fig. 8b,j). Topography analysis shows that the vertical subsidence in the first 30 minutes was lower than the subsequent 30 minutes phases (Fig. 8g,o). In fact, the first sedimentation layer (white sand in the cross-sections, Fig. 7c-d) represents 30 minutes of rifting, and the subsequent layers represents 15 minutes each, resulting in seven fill layers (Fig. 7c-d). Subsidence was slower in models C3 and C4 if compared to models C1 and C2, the first 30 minutes of orthogonal rifting subsidence is comparable with the first 15 minutes in orthogonal rifting. Model C3 and C4 (Fig. 7c,d) did not develop the intra-graben normal faults seen in Models C1 and C2 (Fig. 7a,b).

Orthogonal inversion in Model C3 created initial reverse faulting in the north and SE of the models, but without graben normal fault reactivation (Fig. 8d). By the end of the experiment (Fig. 8e), after 85 minutes, the northern reverse fault became completely inactive while the southern one grew laterally (westward), remaining active. Topography analysis shows uplift limited by the reverse faults lines on both sides of the model (Fig. 8f,h). In cross-section view there is an alternation between north (Fig. 7c$_I$) and south (Fig. 7c$_{II}$) reverse fault activity, and we also observe that reverse faults with larger offsets had an increased thickness.

The oblique inversion in Model C4 (Fig. 8l-m) is predominantly accommodated by a new reverse fault in the south, with limited reactivation of the rift structures. Topography data show additional uplift in the graben in contrast to the orthogonal inversion structures in Model C3 (Fig 8f). The topographic profiles (Fig. 8p) indicate a marked inversion in the graben after the first hour until the end of the experiment. The cross-sections of Models C3 and C4 (Fig. 7c,d) revealed that the reverse fault nucleated in the seed at the base of the graben, and developed a thick shear zone. Section II from Model C3 (Fig. 7c) shows the formation of a reverse fault north of the graben seeding 2 cm below the surface.
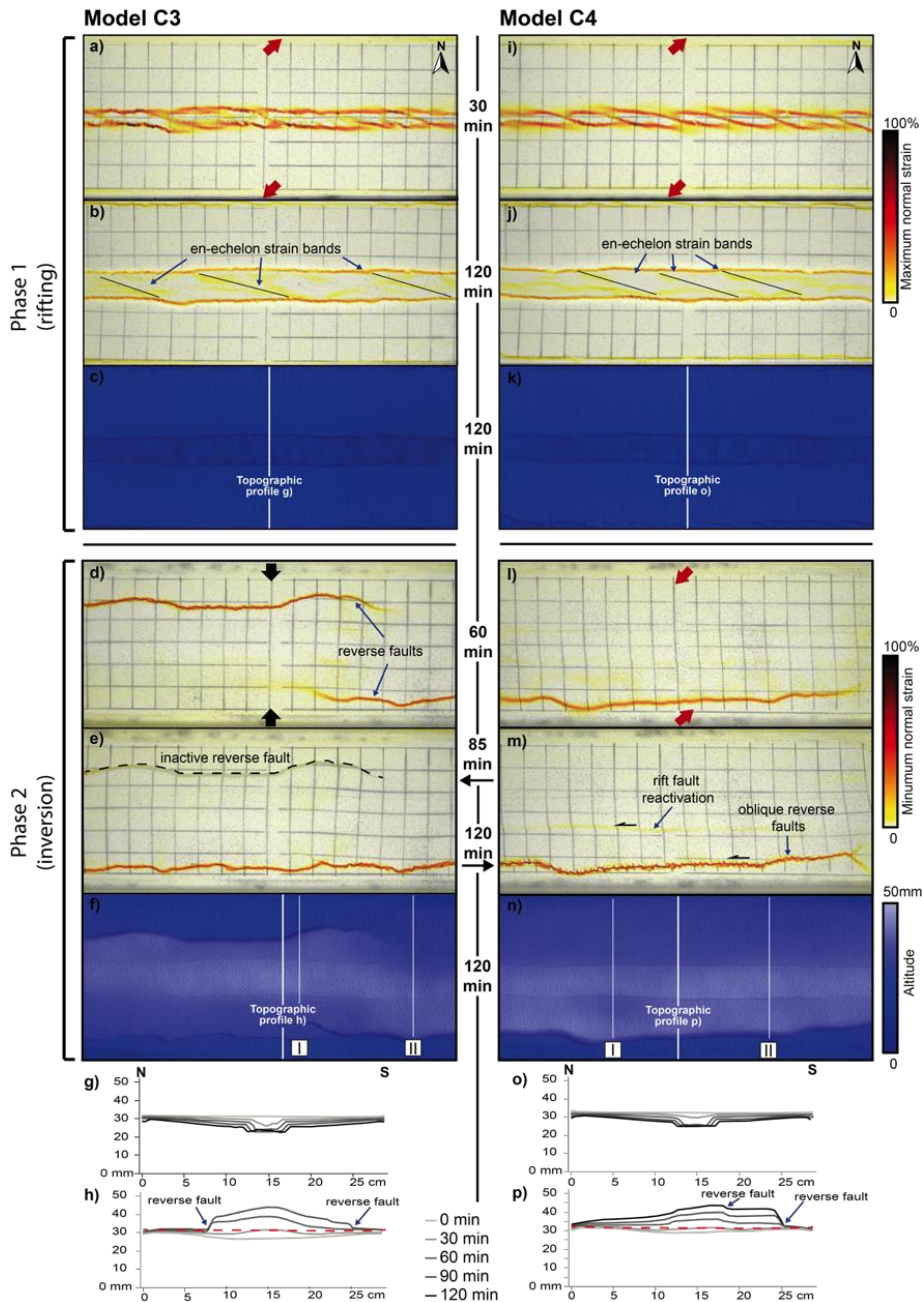
Figure 8: Evolution of deformation during rifting and inversion for Models C3 and C4. a, i) and b, j) displays top view model DIC analysis for Maximum normal strain at early and late rifting stage, resp. c, k) Digital elevation model for late rifting stage. d, l) and e, m) displays top view model DIC analysis for Minimum normal strain. f, n) Digital elevation model for late inversion stage. g, o) Topographic profiles for every 30 minutes of rifting phase. h, p) Topographic profiles for every 30 minutes of inversion phase. Model C3 has a reduced inversion time as indicated in the figure.

410

4 Discussion

4.1 Summary and comparison to previous models

The modeling results, presented in two schematic overview figures (Figs. 9 and 10), show how deformation directions and the presence of syn-rift sedimentation affects initial basin evolution and subsequent inversion.

4.1.1. Rifting phase

The overview of the rifting phase without sedimentation (Fig. 9a and b) shows the general structural differences in graben evolution as a result of different divergence directions ($\alpha = 0°$ and $\alpha = 45°$). The differences in divergence orientation resulted in different initial graben structures. However, at the final stage of rifting the graben geometries were very similar (Fig. 9). The main difference remained within the graben where orthogonal divergence generated parallel pairs of conjugate normal faults, whereas oblique divergence resulted in *en echelon* structures. Furthermore, oblique extension caused a decrease in graben width compared to the orthogonal rifting models, as also described in previous studies (Zwaan and Schreurs, 2016; Zwaan et al., 2018a) (Figs. 3 and 4). This reduction in width is caused by the strike-slip component accommodating deformation in oblique rifting settings.

The syn-rift sedimentation models (Fig. 10a and b) demonstrated the same initial difference in orthogonal and oblique divergence as the models without sedimentation. The oblique divergence models resulted not only in a narrower graben at the end of the extension phase, but also in a reduction of the final total subsidence observed in cross-section (Fig. 7). A narrower graben forming during oblique rift evolution led to smaller loads of sedimentation, consequently there was less weight to cause graben floor subsidence. However, orthogonal and oblique rifting produced a very similar subsidence evolution in response to the syn-rift sedimentation (Fig. 7). The first subsidence interval (I1) was always the smallest, while the subsequent three intervals (I2 to I4) accommodated more subsidence, and from this moment on, sedimentary intervals start thinning again until the last interval (I8). This subsidence rate evolution occurred because the increase in sedimentary load over time enhanced subsidence. However, the reason why we observe a subsidence decline after sedimentation interval I4 remains unclear.

Overall, concerning the total subsidence in models with and without syn-rift sedimentation, we observe that subsidence in the former case was significantly higher while the rift boundary faults remained active for a longer period of time as well. Zwaan et al. (2018a) report a similar basin evolution due to syn-rift sedimentation. In their experiments without syn-rift sedimentation, the absence of sedimentary loading inside the graben leads to a smaller offset along the graben boundary faults since part of the deformation was taken up by intra-graben faults. By contrast, in their models with syn-rift sedimentation, the graben wedge was strengthened, so that faulting remained concentrated along the main graben boundary faults. The latter observation was also made in numerical models by Burov and Poliakov (2001) and Olive et al. (2014).

4.1.2. Inversion phase

455 Our experimental results have established an order of importance regarding the parameters controlling fault reactivation throughout the inversion phase (Figs. 9b and 10b). It seems that the rift kinematics, i.e. orthogonal vs. oblique rifting, have no significant influence on inversion structures as the final rift structures were very similar. Much more important are syn-rift sedimentation and inversion kinematics.

Without sedimentation, the rift structures were reactivated during inversion, and the new reverse faults
460 developed independently of inversion direction (Fig. 9). Both orthogonal and oblique inversion resulted in the development of new reverse faults rooting at the base of the graben (Fig. 9). The reactivation of the rift structures, occurred mainly at the intra graben structures in the orthogonal inversion models (Fig. 4 and 5; Models B1 and B3), whereas in oblique inversion models (Fig. 4 and 5; Models B2 and B4) both the graben boundary faults and the intra-graben faults showed significant reactivation.

465 The presence of syn-rift sediments (Fig. 10b) led to major differences in fault reactivation throughout the inversion phase, since the basin infill acted as a buffer to reactivation of the rift structures. During orthogonal inversion graben faults did not undergo any reactivation while deformation localized in the newly formed reverse faults (Fig. 10). In the oblique inversion models, the reactivation of previous rift structures was observed. Our models results are in accordance with previous studies that described a similar
470 decrease in fault reactivation when syn-rift sedimentation was applied (Pinto et al., 2010b, a; del Ventisette et al., 2006; Panien et al., 2005b; Dubois et al., 2002). By contrast, Panien et al. (2005) found that graben infill increased rift fault reactivation. This difference was likely due to their use of rheologically weak microbeads as graben infill, while we used feldspar and quartz sands so that the graben infill in our models had a similar rheology to the surrounding granular materials. Furthermore, other studies have also show
475 that increasing degrees of oblique compression can promote normal fault reactivation (Nalpas et al., 1995; Brun and Nalpas, 1996). Indeed, while analyzing inverted rift basins, Ziegler et al. (1995) found that in order to facilitate normal fault reactivation the maximum horizontal compressive stress should be at an angle <45° to the normal fault strike.
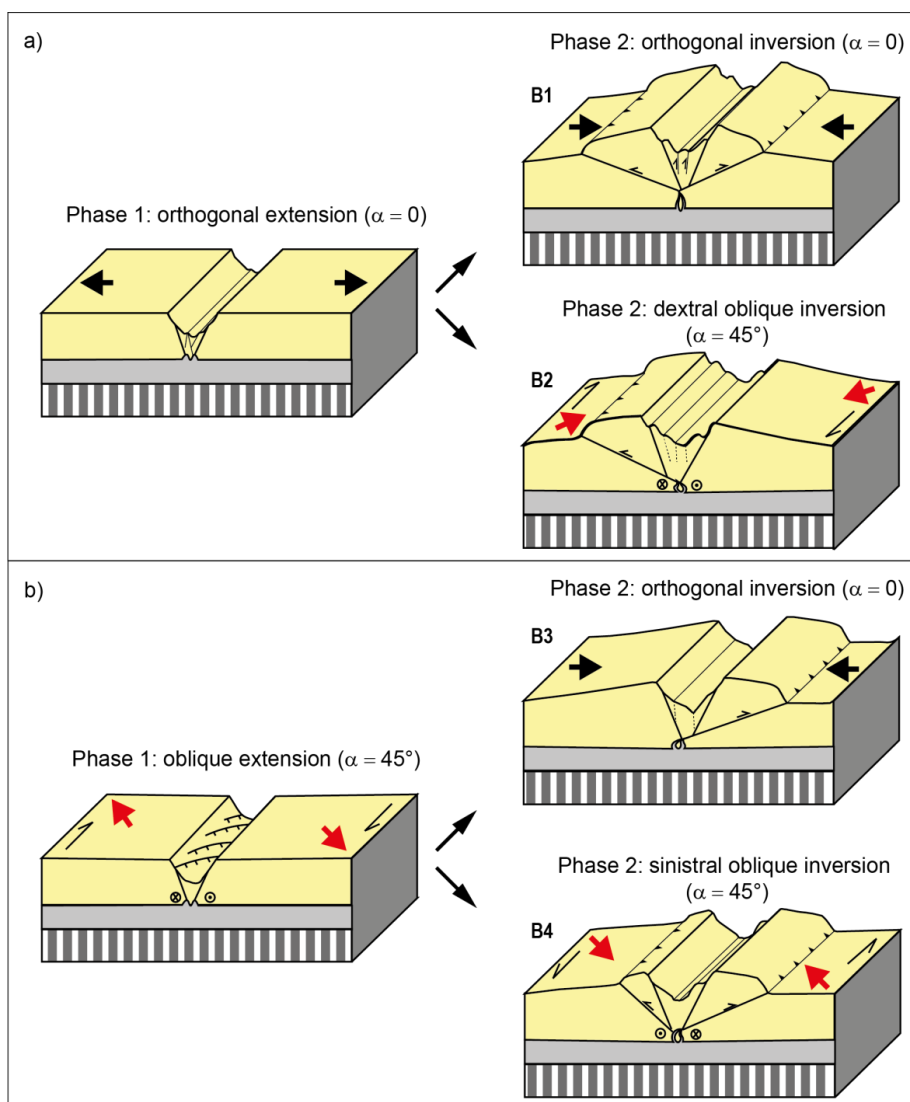
480   **Figure 9: Schematic summary of our experimental results without syn-rift sedimentation**
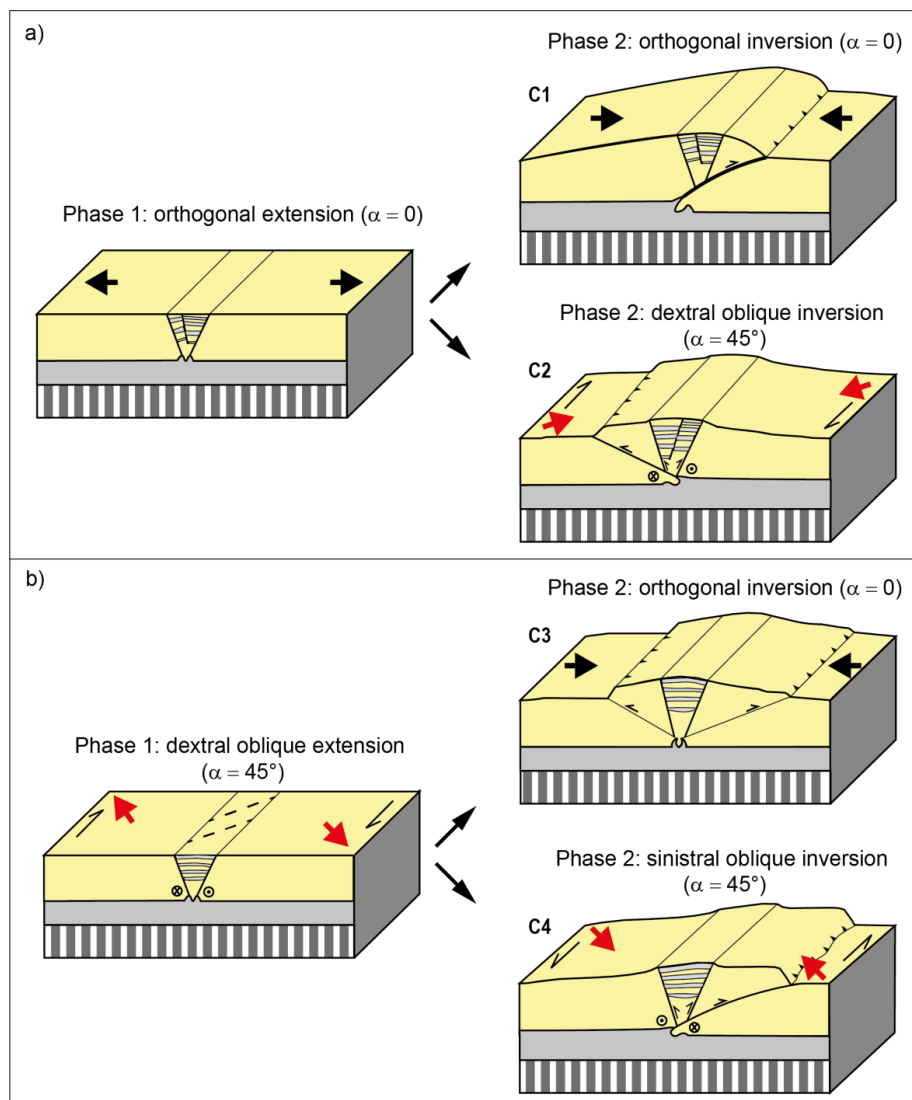
Figure 10: Schematic summary of our experimental results with syn-rift sedimentation

485

4.2 Comparing model results with the Araripe Basin

This study was inspired by the Late Jurassic/Early Cretaceous Araripe Basin in NE Brazil, which is presently situated at 1000 m above sea level (Assine, 2007). This elevation is due to post rift inversion for which two main scenarios have been proposed (rift fault reactivation or regional uplift, Marques et al., 2014 and Peulvast and Bétard, 2015, respectively, Fig. 1). Here we discuss these scenarios in the context of our model results.

Marques et al. (2014) proposed that inversion of the basin resulted from a regional horizontal compression of the South American plate due to the opening of South Atlantic Ocean to the east (ridge-push) and the development of the Andes Cordillera to the west. Furthermore, Marques et al. (2014) concluded that these forces combined were the cause for reactivation and inversion of high angle normal faults. Additionally, the authors stated that the obliquity of the normal faults in relation to the inversion stresses was the facilitator for fault reactivation. However, although we observed some fault reactivation in our oblique inversion models, this reactivation did never lead to full inversion of the graben normal faults (Figs. 9 and 10), which contradicts the Marques et al. (2014) scenario. In fact, no large-scale fault reactivation has been observed in the Araripe Basin (Ponte and Ponte-filho, 1996). A further argument against the Marques et al. (2014) scenario would be that the post-rift sediments outside the original graben domain would not have been uplifted in contrast to what we see in nature (Fig. 1).

This uplift of post rift sediments outside of the original graben domain can be explained by the Peulvast and Bétard (2015) scenario, who proposed a large-scale topographic rather than local basin inversion produced by a regional tectonic uplift (Fig. 1). According to these authors, the present-day high standing mesa formation of the Araripe Basin is the result of differential erosion due to the presence of a strong sandstone formation covering the rift and post-rift sedimentary formations. However, other work demonstrates the continuing compression across the South American plate (Lima, 2003), combined with fault inversion in the region, and suggests that compressional horizontal stresses must have played a role in the Araripe Basin inversion. In fact, recent work shows that mild inversion did take place in the basin (Cardoso, 2010) and also other studies detected inversion in basins from the same rifting system as the Araripe Basin (e.g. Rio do Peixe Basin, Potiguar Basin, Bezerra et al., 2020; Vasconcelos et al., 2021). These authors analysed seismic data and described a mild to moderate tectonic reactivation along the normal faults, however no full-scale basin extrusion is observed. We thus find that neither of the two end-member scenarios seems to fully explain the inversion observed in the Araripe Basin area.

However, we propose an alternative scenario based on our analogue model results (Fig. 11). This scenario involves a basin scale uplift facilitated by newly developed reverse faults rooted at the base of the original graben structure. At the same time, the mild inversion of rift structures is shown to be only possible in oblique compression when syn-rift sediments are present. As such this model can readily explain the field observations from the Araripe Basin but also predicts the presence of large reverse fault, which provides an incentive for further field investigations.
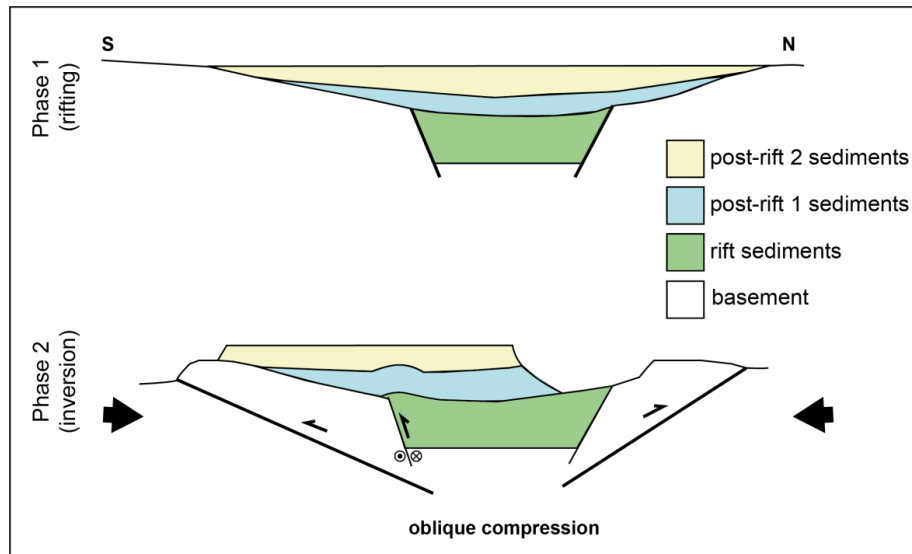
Figure 11: Proposed tectonic evolution of the Araripe Basin inversion based on our analogue model results.

5 Conclusions

In this study we completed a series of new analogue modeling experiments aimed at evaluating the scenarios for basin inversion in the Araripe Basin in NE Brazil (full border fault reactivation vs. regional uplift). We tested the influence of orthogonal (α=0) or oblique (α=45°) extension, followed by either orthogonal or oblique compression on rift development and on subsequent inversion structures. We find that:

- During rifting without sedimentation orthogonal extension creates through-going border faults, whereas oblique extension leads to the initial formation of en-echelon faults that eventually will link up to establish large border faults. Rift basins with syn-rift sedimentation follow a similar evolution, however the sedimentary loading causes increase subsidence compared to models without sedimentation.

- During inversion, a major part of the deformation is accommodated by newly formed low angle reverse faults. Within that framework, models without sedimentation saw significant intra-graben fault reactivation, roughly independent of inversion direction (α=0 or α=45°). By contrast, in models with syn-rift sedimentation, inversion caused only minor reactivation of the original rift faults during oblique compression, due to the sedimentary infill acting as buffer during compression. Orthogonal compression in models with syn-rift sediments did not lead to rift fault reactivation.

- An assessment of the existing scenarios for inversion in the Araripe basin with our model results as well as data from the field show that these scenarios do not fully explain all observations of the natural example. Therefore, based on our model results we propose an alternative scenario involving oblique compression and the development low angle reverse faults. This scenario better explains the available field observations in the Araripe Basin but also provides and incentive for future (field) studies.

Authors contributions

PCR, FZ and GS planned and designed the experiments. PCR completed the experiments, analysed the model results, and wrote the first manuscript draft. FZ participated in running some of the experiments. FZ and TCS helped performing the model analysis. PCR, FZ, GS, RSS, TCS participated in the interpretation of the model results, and reviewed and edited the manuscript.

Competing interests

The authors declare that they have no conflict of interest.

Acknowledgements

PCR and RSS gratefully acknowledge the support from research and development project "Correlação
565   estratigráfica, evolução paleoambiental e paleogeográfica e perspectivas exploratórias do Andar Alagoas",
sponsored by Shell Brasil Petróleo Ltda, and the strategic importance of the support given by ANP (Brazil's
National Oil, Natural Gas and Biofuels Agency) through the R&D levy regulation (Technical Cooperation
#20.219-2). PCR acknowledges CAPES – Coordination for the Improvement of Higher Education
Personnel – for their financial support. FZ and TCS were funded by the Swiss National Science Foundation
570   (via grant 200021-178731, https://data.snf.ch/grants/grant/178731, awarded to GS), which also covered the
Open Access publication costs. RSS acknowledges CNPq n° 311748/2018-0, FAPERJ n° E-
26/200.995/2021   and   Swiss   National   Science   Foundation   n°   IZSEZ0_191196/1
(https://data.snf.ch/grants/grant/191196) research grants. We thank Florian Ott and Kirsten Elger for
helping us creating a GFZ data publication containing supplementary material (Richetti et al. in prep).

575

Data availability

Detailed overviews of model results are made publicly available in the form of a GFZ data publication
(Richetti et al. in prep).

Temporary link: https://1drv.ms/u/s!AnD2tls1Utsrg_8b10PsZiOu7qn1Yw?e=KLkOdi

580   Example of GFZ data publication: https://doi.org/10.5880/fidgeo.2021.042

References

Adam, J., Urai, J. L., Wieneke, B., Oncken, O., Pfeiffer, K., Kukowski, N., Lohrmann, J., Hoth, S., van der Zee, W., and Schmatz, J.: Shear localisation and strain distribution during tectonic faulting—new insights from granular-flow experiments and high-resolution optical image correlation techniques, J Struct Geol, 27, 283–301, https://doi.org/10.1016/j.jsg.2004.08.008, 2005.

Assine, M. L.: Bacia do Araripe, Boletim de Geociências da Petrobras, 15, 371–389, 2007.

Bezerra, F. H., de Castro, D. L., Maia, R. P., Sousa, M. O. L., Moura-Lima, E. N., Rossetti, D. F., Bertotti, G., Souza, Z. S., and Nogueira, F. C. C.: Postrift stress field inversion in the Potiguar Basin, Brazil – Implications for petroleum systems and evolution of the equatorial margin of South America, Mar Pet Geol, 111, 88–104, https://doi.org/10.1016/J.MARPETGEO.2019.08.001, 2020.

Boutelier, D., Schrank, C., and Regenauer-Lieb, K.: 2-D finite displacements and strain from particle imaging velocimetry (PIV) analysis of tectonic analogue models with TecPIV, Solid Earth, 10, 1123–1139, https://doi.org/10.5194/se-10-1123-2019, 2019.

Brito Neves, B. B., Santos, E. J., and van Schmus, W. R.: Tectonic history of the Borborema province, northeastern Brazil, in: 31st International Geological Congress, 151–182, 2000.

Broerse, T., Krstekanić, N., Kasbergen, C., and Willingshofer, E.: Mapping and classifying large deformation from digital imagery: application to analogue models of lithosphere deformation, Geophys J Int, 226, 984–1017, https://doi.org/10.1093/gji/ggab120, 2021.

Brun, J.-P. and Nalpas, T.: Graben inversion in nature and experiments, Tectonics, 15, 677–687, https://doi.org/10.1029/95TC03853, 1996.

Buck, W. R.: Modes of continental lithospheric extension, J Geophys Res Solid Earth, 96, 20161–20178, https://doi.org/10.1029/91JB01485, 1991.

Byerlee, J.: Friction of Rocks, in: Rock Friction and Earthquake Prediction, edited by: Byerlee, J. D. and Wyee, M., Birkhäuser Basel, Basel, 615–626, https://doi.org/10.1007/978-3-0348-7182-2_4, 1978.

Camacho, C. R., Oliveira e Souza, F. R. F. R.: O arcabouço estrutural da Bacia Sedimentar do Araripe, Província Borborema, baseado em dados aeromagnetométricos, Geol. USP, Série científica, 17, 3, 149-161, https://10.11606/issn.2316-9095.v17-393, 20

Cardoso, F. M. C.: O graben da Palestina: contribuição à estratigrafia e estrutura do estágio rifte na Bacia do Araripe, Nordeste do Brasil, Universidade Federal do Rio Grande do Norte, Natal, 1–129 pp., 2010.

di Domenica, A., Petricca, P., Trippetta, F., Carminati, E., and Calamita, F.: Investigating fault reactivation during multiple tectonic inversions through mechanical and numerical modeling: An application to the Central-Northern Apennines of Italy, J Struct Geol, 67, 167–185, https://doi.org/10.1016/j.jsg.2014.07.018, 2014.

Dubois, A., Odonne, F., Massonnat, G., Lebourg, T., and Fabre, R.: Analogue modelling of fault reactivation: tectonic inversion and oblique remobilisation of grabens, J Struct Geol, 24, 1741–1752, https://doi.org/10.1016/S0191-8141(01)00129-8, 2002.

Ganade de Araujo, C. E., Weinberg, R. F., and Cordani, U. G.: Extruding the Borborema Province (NE-Brazil): A two-stage Neoproterozoic collision process, Terra Nova, 26, 157–168, https://doi.org/10.1111/ter.12084, 2014.

Hubbert, M. K.: Theory of scale models as applied to the study of geologic structures, Geol Soc Am Bull, 48, 1459–1520, https://doi.org/10.1130/GSAB-48-1459, 1937.

Jara, P., Likerman, J., Charrier, R., Herrera, S., Pinto, L., Villarroel, M., and Winocur, D.: Closure type effects on the structural pattern of an inverted extensional basin of variable width: Results from analogue models, J South Am Earth Sci, 87, 157–173, https://doi.org/10.1016/j.jsames.2017.10.018, 2018.

625   Klinkmüller, M., Schreurs, G., Rosenau, M., and Kemnitz, H.: Properties of granular analogue model materials: A community wide survey, Tectonophysics, 684, 23–38, https://doi.org/10.1016/j.tecto.2016.01.017, 2016.

Lamarque, G. and Julià, J.: Lithospheric and sub-lithospheric deformation under the Borborema Province of NE Brazil from receiver function harmonic stripping, Solid Earth Discussions, 1–20,
630   https://doi.org/10.5194/se-2019-41, 2019.

Lima, C.: Ongoing compression across South American plate: observations, numerical modelling and some implications for petroleum geology, Geological Society, London, Special Publications, 209, 87–100, https://doi.org/10.1144/GSL.SP.2003.209.01.09, 2003.

Maestrelli, D., Montanari, D., Corti, G., del Ventisette, C., Moratti, G., and Bonini, M.: Exploring the
635   Interactions Between Rift Propagation and Inherited Crustal Fabrics Through Experimental Modeling, Tectonics, 39, https://doi.org/10.1029/2020TC006211, 2020.

Marques, F. O., Nogueira, F. C. C., Bezerra, F. H. R., and de Castro, D. L.: The Araripe Basin in NE Brazil: An intracontinental graben inverted to a high-standing horst, Tectonophysics, 630, 251–264, https://doi.org/10.1016/j.tecto.2014.05.029, 2014.

640   Marshak, S., Haq, S. S. B., and Sen, P.: Ramp initiation in fold-thrust belts: Insight from PIV analysis of sandbox models, J Struct Geol, 118, 308–323, https://doi.org/10.1016/j.jsg.2018.11.006, 2019.

de Matos, R. M. D.: The Northeast Brazilian Rift System, Tectonics, 11, 766–791, https://doi.org/10.1029/91TC03092, 1992.

Molnar, N., Cruden, A., and Betts, P.: The role of inherited crustal and lithospheric architecture during
645   the evolution of the Red Sea: Insights from three dimensional analogue experiments, Earth Planet Sci Lett, 544, 116377, https://doi.org/10.1016/j.epsl.2020.116377, 2020.

Molnar, N. E., Cruden, A. R., and Betts, P. G.: Interactions between propagating rifts and linear weaknesses in the lower crust, Geosphere, 15, 1617–1640, https://doi.org/10.1130/GES02119.1, 2019.

Moulin, M., Aslanian, D., and Unternehr, P.: A new starting point for the South and Equatorial Atlantic
650   Ocean, Earth Sci Rev, 98, 1–37, https://doi.org/10.1016/j.earscirev.2009.08.001, 2010.

Mulugeta, G.: Squeeze box in a centrifuge, Tectonophysics, 148, 323–335, https://doi.org/10.1016/0040-1951(88)90139-4, 1988.

Nalpas, T., le Douaran, S., Brun, J. P., Unternehr, P., and Richert, J. P.: Inversion of the Broad Fourteens Basin (offshore Netherlands), a small-scale model investigation, Sediment Geol, 95, 237–250,
655   https://doi.org/10.1016/0037-0738(94)00113-9, 1995.

Neto, F. L. S., Julià, J., and Schimmel, M.: Upper-mantle structure of the Borborema Province, NE Brazil, from P-wave tomography: Implications for rheology and volcanism, Geophys J Int, 216, 231–250, https://doi.org/10.1093/gji/ggy421, 2019.

Panien, M., Schreurs, G., and Pfiffner, A.: Sandbox experiments on basin inversion: Testing the influence
660   of basin orientation and basin fill, J Struct Geol, 27, 433–445, https://doi.org/10.1016/j.jsg.2004.11.001, 2005.

Panien, M., Schreurs, G., and Pfiffner, A.: Mechanical behaviour of granular materials used in analogue modelling: insights from grain characterisation, ring-shear tests and analogue experiments, J Struct Geol, 28, 1710-1724, https://doi.org/10.1016/j.jsg.2006.05.004, 2006.

665   Peulvast, J. P. and Bétard, F.: A history of basin inversion, scarp retreat and shallow denudation: The Araripe basin as a keystone for understanding long-term landscape evolution in NE Brazil, Geomorphology, 233, 20–40, https://doi.org/10.1016/j.geomorph.2014.10.009, 2015.

Pinto, L., Muñoz, C., Nalpas, T., and Charrier, R.: Role of sedimentation during basin inversion in analogue modelling, J Struct Geol, 32, 554–565, https://doi.org/10.1016/J.JSG.2010.03.001, 2010a.

670   Ramberg, H.: Gravity, Deformation and the Earth's Crust, Academic Press, London, 1981.

Rebelo, T. B., Batezelli, A., and Luna, J. S.: Stratigraphic evolution and carbonate factory implications: Case study of the Albian carbonates of the Campos Basin, Brazil, The Depositional Record, 7, 271–293, https://doi.org/10.1002/dep2.118, 2021.

Richetti, P. C., Zwaan, F., Schreurs, G., Schmitt, R. S., Schmid, T. C.: Overviews and videos of top view
675   imagery, topography data and DIC analysis results from analogue models of basin inversion. GFZ Data Services, in prep.

Schmid, T. C., Schreurs, G., and Adam, J.: Characteristics of continental rifting in rotational systems: New findings from spatiotemporal high resolution quantified crustal scale analogue models, Tectonophysics, 822, 229174, https://doi.org/10.1016/J.TECTO.2021.229174, 2022.

680   Schmid, T., Schreurs, G., Warsitzka, M., and Rosenau, M.: Effect of sieving height on density and friction of brittle analogue material: Ring-shear test data of quarz sand used for analogue experiments in the Tectonic Modelling Lab of the University of Bern, 2020.

Schreurs, G. and Colletta, B.: Analogue modelling of faulting in zones of continental transpression and transtension, Geological Society, London, Special Publications, 135, 59–79,
685   https://doi.org/10.1144/GSL.SP.1998.135.01.05, 1998.

Schreurs, G. and Colletta, B.: Analogue modelling of continental transpression, Journal of the Virtual Explorer, 07, https://doi.org/10.3809/jvirtex.2002.00040, 2002.

Sibson, R. H. and Scott, J.: Stress/fault controls on the containment and release of overpressured fluids: Examples from gold-quartz vein systems in Juneau, Alaska; Victoria, Australia and Otago, New Zealand,
690   Ore Geol Rev, 13, 293–306, https://doi.org/10.1016/S0169-1368(97)00023-1, 1998.

Stanton, N., Ponte-Neto, C., Bijani, R., Masini, E., Fontes, S., and Flexor, J.-M.: A geophysical view of the Southeastern Brazilian margin at Santos Basin: Insights into rifting evolution, J South Am Earth Sci, 55, 141–154, https://doi.org/10.1016/j.jsames.2014.07.003, 2014.

Turner, J. P. and Williams, G. A.: Sedimentary basin inversion and intra-plate shortening, Earth Sci Rev,
695   65, 277–304, https://doi.org/10.1016/J.EARSCIREV.2003.10.002, 2004.

Vasconcelos, D. L., Marques, F. O., Nogueira, F. C. C., Perez, Y. A. R., Bezerra, F. H. R., Stohler, R. C., and Souza, J. A. B.: Tectonic inversion assessed by integration of geological and geophysical data: The intracontinental Rio do Peixe Basin, NE Brazil, Basin Research, 33, 705–728, https://doi.org/10.1111/bre.12491, 2021.

700   Vauchez, A., Neves, S., Caby, R., Corsini, M., Egydio-Silva, M., Arthaud, M., and Amaro, V.: The Borborema shear zone system, NE Brazil, J South Am Earth Sci, 8, 247–266, https://doi.org/10.1016/0895-9811(95)00012-5, 1995.

del Ventisette, C., Montanari, D., Bonini, M., and Sani, F.: Positive fault inversion triggering "intrusive diapirism": An analogue modelling perspective, Terra Nova, 17, 478–485, https://doi.org/10.1111/j.1365-
705   3121.2005.00637.x, 2005.

del Ventisette, C., Montanari, D., Sani, F., and Bonini, M.: Basin inversion and fault reactivation in laboratory experiments, J Struct Geol, 28, 2067–2083, https://doi.org/10.1016/J.JSG.2006.07.012, 2006.

Weijermars, R. and Schmeling, H.: Scaling of Newtonian and non-Newtonian fluid dynamics without inertia for quantitative modelling of rock flow due to gravity (including the concept of rheological
710   similarity), Physics of the Earth and Planetary Interiors, 43, 316–330, https://doi.org/10.1016/0031-9201(86)90021-X, 1986.

Ziegler, P. A., Cloetingh, S., and van Wees, J.-D.: Dynamics of intra-plate compressional deformation: the Alpine foreland and other examples, Tectonophysics, 252, 7–59, https://doi.org/10.1016/0040-1951(95)00102-6, 1995.

715   Zwaan, F. and Schreurs, G.: How oblique extension and structural inheritance influence rift segment interaction: Insights from 4D analog models, Interpretation, 5, SD119–SD138, https://doi.org/10.1190/INT-2016-0063.1, 2016.

Zwaan, F. and Schreurs, G.: How oblique extension and structural inheritance influence rift segment interaction: Insights from 4D analog models, Interpretation, 5, SD119–SD138,
720   https://doi.org/10.1190/INT-2016-0063.1, 2017.

Zwaan, F., Schreurs, G., Naliboff, J., and Buiter, S. J. H.: Insights into the effects of oblique extension on continental rift interaction from 3D analogue and numerical models, Tectonophysics, 693, 239–260, https://doi.org/10.1016/j.tecto.2016.02.036, 2016.

Zwaan, F., Schreurs, G., and Adam, J.: Effects of sedimentation on rift segment evolution and rift
725   interaction in orthogonal and oblique extensional settings: Insights from analogue models analysed with 4D X-ray computed tomography and digital volume correlation techniques, Glob Planet Change, 171, 110–133, https://doi.org/10.1016/j.gloplacha.2017.11.002, 2018a.

Zwaan, F., Schreurs, G., Ritter, M., Santimano, T., and Rosenau, M.: Rheology of PDMS-corundum sand mixtures from the Tectonic Modelling Lab of the University of Bern (CH), GFZ Data Services, 1, 2018b.

730   Zwaan, F., Schreurs, G., and Rosenau, M.: Rift propagation in rotational versus orthogonal extension: Insights from 4D analogue models, J Struct Geol, 135, 103946, https://doi.org/10.1016/J.JSG.2019.103946, 2020.

Zwaan, F., Schreurs, G., Buiter, S., Ferrer, O., Reitano, R., Rudolf, M., and Willingshofer, E.: Analogue modelling of basin inversion: a review and future perspectives, Solid Earth Discussions, 2022, 1–84,
735   https://doi.org/10.5194/se-2022-8, 2022.